Morphology and dynamics of star dunes from numerical modelling

Deguo Zhang[1], Clément Narteau[1],
Olivier Rozier[1], Sylvain Courrech du Pont[2]

[1] Equipe de Dynamique des Fluides Géologiques, Institut de Physique du Globe de Paris, Sorbonne Paris Cité, Univ Paris Diderot, UMR 7154 CNRS, 1 rue Jussieu, 75238 Paris Cedex 05, France.

[2] Laboratoire Matière et Système Complexes, Sorbonne Paris Cité, Univ Paris Diderot, UMR 7057 CNRS, Bâtiment Condorcet, 10 rue Alice Domon et Léonie Duquet, 75205 Paris Cedex 13, France.

Contents

Figure 1: The three states (fluid, mobile and immobile sediment) and the doublet interactions in the model of sediment transport. Different sets of transition are associated with deposition, erosion, transport, gravity and diffusion. $\{\Lambda_c,\ \Lambda_e,\ \Lambda_t,\ \Lambda_g,\ \Lambda_d\}$ are transition rates with units of frequency; a and b are constants (see Tab. 1 for the model parameter values). The central inset shows the direction of the flow and the orientation of the nearest neighbours in our regular cubic lattice. Neutral cells are used to shape the virtual environment. Injection/removal cells are used to introduce input/output fluxes of sediment.

The different ingredients of the model summarised in Secs. 1 and 2 have been described in full details in *Narteau et al.* [2009]. We just recall here the main characteristics which are particularly relevant to the present study. In addition, we present how we extract the transport properties from the wind data. Finally, in Sec. 3 we detail how we analyse the morphodynamics of star dune for different T_θ-values, the period of wind directionality.

1 Sediment transport, flow calculation and wind speed in the real-space cellular automaton model

In the model of sediment transport, we consider three states (fluid, mobile and immobile sediment) and local interactions between pairs of nearest neighbour cells called doublets (Fig. 1). We isolate individual physical processes and associate each of them with a set of doublet transitions and a specific transition rate. This way, we introduce into the model the characteristic time scales of the physical mechanisms under consideration (erosion, transport, deposition, gravity and diffusion). Neutral cells are used to shape the virtual environment. Here, the sedimentary cells are placed on a rotating table to reproduce all types of wind directionality (Fig. 1 of the main

2

manuscript).

Elementary units		Units
l_0	Length	$[L]$
t_0	Time	$[T]$
τ_0	Stress	$[M][L]^{-1}[T]^{-2}$

Model parameters		Units	Value
L	System width and length	l_0	$[400, 600]$
H	System height	l_0	100
Λ_0	Transition rate for erosion	$1/t_0$	1
Λ_t	Transition rate for transport	$1/t_0$	1.5
Λ_c	Transition rate for deposition	$1/t_0$	0.5
Λ_g	Transition rate for gravity	$1/t_0$	10^5
Λ_d	Transition rate for diffusion	$1/t_0$	0.01
a	Erosion/transport coefficient	1	0.1
b	Deposition coefficient	1	10
$\tau_2 - \tau_1$	Erosion range	τ_0	100

Table 1: Units and values of the parameters of the model of sediment transport.

We use a two-dimensional lattice-gas model to simulate the flow and calculate the permanent feedback between bed shear stress and topography [*Frisch et al.*, 1986; *d'Humières et al.*, 1986; *Chopard and Droz*, 1998; *Rothman and Zaleski*, 2004]. In the model of sediment transport, the flow is calculated in 2D vertical planes parallel to the direction of the wind and confined by two walls of neutral cells at the top and the bottom of the system.

Using the output of the lattice-gas cellular automaton, we estimate both components of the local velocity field by averaging the velocity vectors of fluid particles over space and time. Velocity $\overrightarrow{V}$ is expressed in terms of a number of fluid particles and we use the normal $\overrightarrow{n}$ to the topography to calculate the bed shear stress

$$\tau_s = \tau_0 \frac{\partial \overrightarrow{V}}{\partial \overrightarrow{n}}, \tag{1}$$

where τ_0 is the stress scale of the model (see Tab. 1). Then, we consider that the erosion rate is linearly related to the bed shear stress τ_s according to

$$\Lambda_e = \begin{cases} 0 & \text{for } \tau_s \leq \tau_1, \\ \Lambda_0 \dfrac{\tau_s - \tau_1}{\tau_2 - \tau_1} & \text{for } \tau_1 \leq \tau_s \leq \tau_2, \\ \Lambda_0 & \text{else.} \end{cases} \tag{2}$$

3

where Λ_0 is a constant rate, τ_1 is the threshold for motion inception and τ_2 is a parameter to adjust the linear relationship. By definition, $(\tau_s - \tau_1)$ is the excess shear stress from which we can account for the feedback mechanism of the bed shear stress on the topography.

In the simulations presented here, all the model parameter values are kept constant except the T_θ-value. Nevertheless, we can associate changes in τ_1-values to variations in excess shear stress and therefore to variations in wind shear velocity: the higher the τ_1-value is, the lower the wind shear velocity is. Then, for all τ_1-values, we have computed the saturated sand flux on a flat bed and renormalise this flux with respect to its maximum value at $\tau_1 = 0$ (Fig. 2).
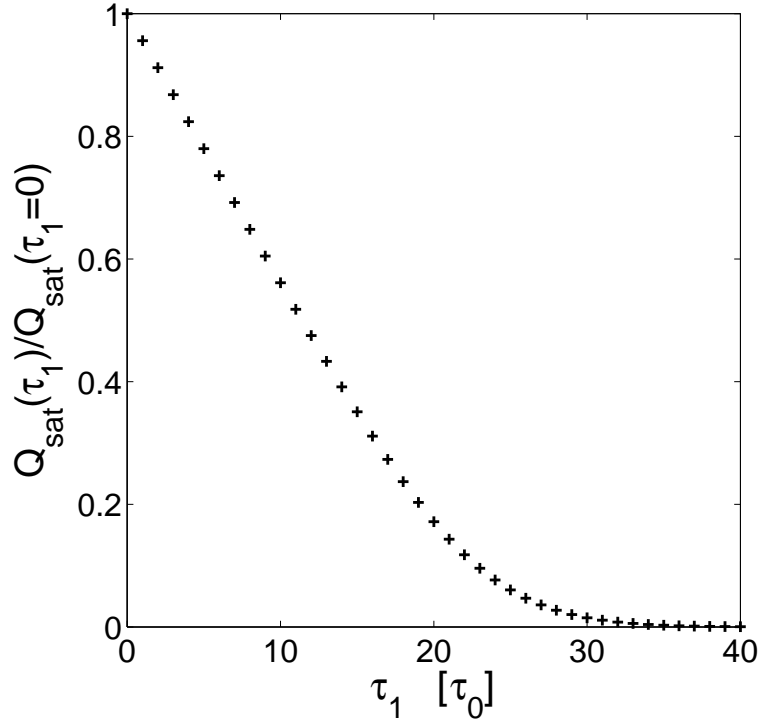
Figure 2: The saturated flux with respect to the τ_1-value. $Q_{\mathrm{sat}}(\tau_1)$ is normalised by its maximum value $Q_{\mathrm{sat}}(\tau_1 = 0)$. Note that an increasing τ_1-value corresponds to a decreasing flow strength and that these changes in τ_1-value do not affect the spatial and temporal distributions of the bed shear stress τ_s on an arbitrary flat layer of sediment.

Theoretical transport relationships can be expressed as

$$Q_{\mathrm{sat}} = \begin{cases} 0 & \text{if } \tau_s \leq \tau_{\mathrm{c}}, \\ \tau_s^{\gamma}(\tau_s - \tau_{\mathrm{c}}) & \text{if } \tau_s \geq \tau_{\mathrm{c}}. \end{cases}$$

where γ is a positive (or null) constant and τ_{c} the shear stress at the onset of erosion [*Bagnold*, 1956; *Anderson and Haff*, 1988; *Ungar and Haff*, 1987;

4

Rasmussen et al., 1996; *Andreotti*, 2004]. Introducing the shear velocity $u_* \propto \tau_s^{1/2}$ (i. e. high Reynolds number) and considering that Q_{sat}^0 is the Q_{sat}-value for $\tau_{\mathrm{c}} = 0$, we can show that

$$\frac{Q_{\mathrm{sat}}}{Q_{\mathrm{sat}}^0} = 1 - \left(\frac{u_{\mathrm{c}}}{u_*}\right)^2. \tag{3}$$

As described below, wind velocity time series allow to calculate the (u_*/u_{c})-value in nature and therefore to estimate the corresponding $Q_{\mathrm{sat}}/Q_{\mathrm{sat}}^0$-value. Considering that we have the same ratio in the model, Eq. 3 and Fig. 2 give the opportunity to estimate the τ_1-value that we should take in our simulation. This value corresponds to a given flux of sediment $Q_{\mathrm{sat}}(\tau_1)$ expressed in units of l_0^2/t_0, where l_0 and t_0 are the elementary length and time scales of the model, respectively. Let us now determine the $\{l_0, t_0\}$-values.

2   Length and time scales in the real-space cellular automaton dune model

The elementary length and time scales $\{l_0, t_0\}$ of the real-space cellular automaton dune model are determined with respect to the physical mechanism that select λ_{max}, the characteristic length scales for the formation of dunes in nature (i. e. the most unstable wavelength of a flat sand bed exposed to a fluid flow). Then, in all natural environments where the dune instability can be observed, the l_0 and t_0-values can be calculated with respect to the magnitude of the parameters that control the λ_{max}-value and the saturated flux of sediment [*Hersen et al.*, 2002; *Elbelrhiti et al.*, 2005; *Charru*, 2006; *Claudin and Andreotti*, 2006; *Narteau et al.*, 2009; *Zhang et al.*, 2010].

2.1   The elementary length scale

Using a linear stability analysis, the characteristic length scale for the formation of dunes in the model, λ_{max}, can be expressed in unit of l_0 and compare to the corresponding length scale in nature. For arid desert on Earth, *Elbelrhiti et al.* [2005] have shown that

$$\lambda_{\mathrm{max}} \approx 50 \, \frac{\rho_{\mathrm{s}}}{\rho_{\mathrm{f}}} d \approx 20\,\mathrm{m}.$$

In the cellular automaton dune model, *Narteau et al.* [2009] have shown that

$$\lambda_{\mathrm{max}} \approx 40 \, l_0.$$

Then, the elementary length scale of the real-space cellular automaton dune model is

$$l_0 = 0.5\,\mathrm{m}. \tag{4}$$

5

2.2 The elementary time scale

From the meteorological data-file of Hassi-Messaoud airport (Algeria, 31º 40'
North, 6º 9' East), we extract the wind speed u^i and the wind direction $\overrightarrow{x_i}$
at different times $t_1 \leq t_i \leq t_N$, $i \in [1, N]$. Considering that these wind
properties have been measured at a height of $z = 10\,\mathrm{m}$, we calculate the
shear velocity

$$u_*^i = \frac{u^i \kappa}{\log(z/z_0)}$$

where $z_0 = 10^{-3}\,\mathrm{m}$ is the surface roughness length and $\kappa = 0.4$ is the von-
Kármán constant. The mean shear velocity is

$$\langle u_* \rangle = \frac{\displaystyle\sum_{i=2}^{N} u_*^i \delta_i(t_i - t_{i-1})}{\displaystyle\sum_{i=2}^{N} \delta_i(t_i - t_{i-1})},$$

with

$$\delta_i = \begin{cases} 0 & \text{for } u_*^i < u_{\mathrm{c}}, \\ 1 & \text{for } u_*^i \geq u_{\mathrm{c}}. \end{cases}$$

We obtain

$$\langle u_* \rangle = 0.33 \text{ m/s} \qquad \text{and} \qquad \left\langle \frac{u_*}{u_{\mathrm{c}}} \right\rangle = 1.72$$

using the formula of *Iversen and Rasmussen* [1999],

$$u_{\mathrm{c}} = 0.1 \sqrt{\frac{\rho_s}{\rho_f} g d} = 0.19 \text{ m/s},$$

to determine the threshold shear velocity value for motion inception. Then,
we inject this $\langle u_*/u_{\mathrm{c}} \rangle$-value in Eq. 3 and Fig. 2 to estimate the corresponding
τ_1-value and the corresponding flux of sediment. Here, we have

$$\frac{Q_{\mathrm{sat}}(\tau_1)}{Q_{\mathrm{sat}}(\tau_1 = 0)} = 0.66,$$

$$\tau_1 = 8\tau_0 \qquad \text{and} \qquad Q_{\mathrm{sat}} = 0.44 \, l_0^2/t_0.$$

With the same wind data, we also estimate the sand flux using another
relationship proposed by *Iversen and Rasmussen* [1999],

$$Q_{\mathrm{sat}}(u_*) = 22 \frac{\rho_f}{\rho_s} \sqrt{\frac{d}{g}} \left(u_*^2 - u_c^2 \right) \qquad \text{for} \quad u_* \geq u_{\mathrm{c}}.$$

6

In practice, we calculate the sand flux vector over a flat sand bed

$$\overrightarrow{Q^i_{sat}} = Q_{\text{sat}}(u^i_*)\delta_i \overrightarrow{x_i}.$$

Thus, we estimate the mean sand flux, also called the drift potential,

$$Q = DP = \frac{\sum\limits_{i=2}^{N} \|\overrightarrow{Q^i_{sat}}\|(t_i - t_{i-1})}{\sum\limits_{i=2}^{N}(t_i - t_{i-1})} = 48\,\text{m}^2/\text{a},$$

as well as the resultant drift potential

$$RDP = \left\| \sum_{i=2}^{N}(t_i - t_{i-1})\overrightarrow{Q^i_{sat}} \right\| = 7.8\,\text{m}^2/a$$

from the 1$^{\text{st}}$ of January 2006 to the 31$^{\text{st}}$ of December 2009.

Finally, matching the average saturated flux in the model to the mean saturated flux in the dunefield, we get

$$t_0 = \frac{Q_{\text{sat}}(\tau_1)}{Q} l_0^2.$$

Numerically, we obtain

$$t_0 = 2.3 \ 10^{-3} \text{ a} = 0.84 \text{ d} = 20.17 \text{ h}.$$

2.3 Model parameters

An important ingredient of the model is that each transition is characterised by a rate parameter with the dimension of a frequency. These transition rates introduce into the model the characteristic time scales of the physical mechanisms under consideration (Tab. 1).

All these rate parameters are expressed with respect to the elementary time scale t_0 in such a way that their relative contribution have to be measured from their ratio. For this reason, transition rates for erosion (Λ_0), deposition (Λ_c) and transport (Λ_t) are chosen close to one with $\Lambda_c < \Lambda_0 < \Lambda_t$. Gravity ($\Lambda_g$) and diffusion ($\Lambda_d$) are occurring over much shorter and longer periods of time, respectively. We chose $\Lambda_d \ll \Lambda_0 \ll \Lambda_g$. $a < 1$ corresponds to the ratio between vertical and horizontal transition rates for erosion and transport; $b > 1$ corresponds to the ratio between deposition rates on flat and rough surfaces (see Fig. 1).
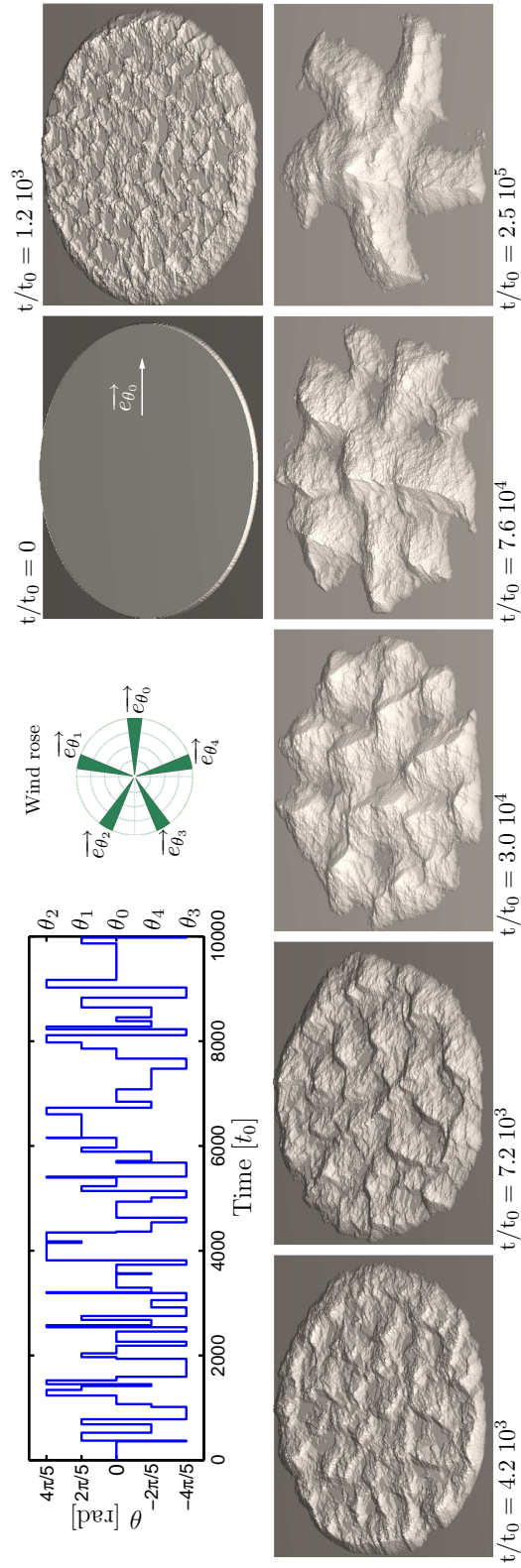
Figure 3: Formation of a star dune by coarsening using a random time function $\theta(t)$ of wind directionality. The wind blows from 5 directions ($\theta_i = 2\pi i/5$, with $i \in \{0, 1, 2, 3, 4\}$), as shown by the wind rose. The mean time spent in each direction is the same and the wind speed is constant ($T_\theta = 5t_\theta = 500 \, t_0$). Thus, winds are equally balanced and the mean wind is null. The final stage shows the star dune in a dynamic equilibrium state that is reached when dune height scales with flow depth.

8
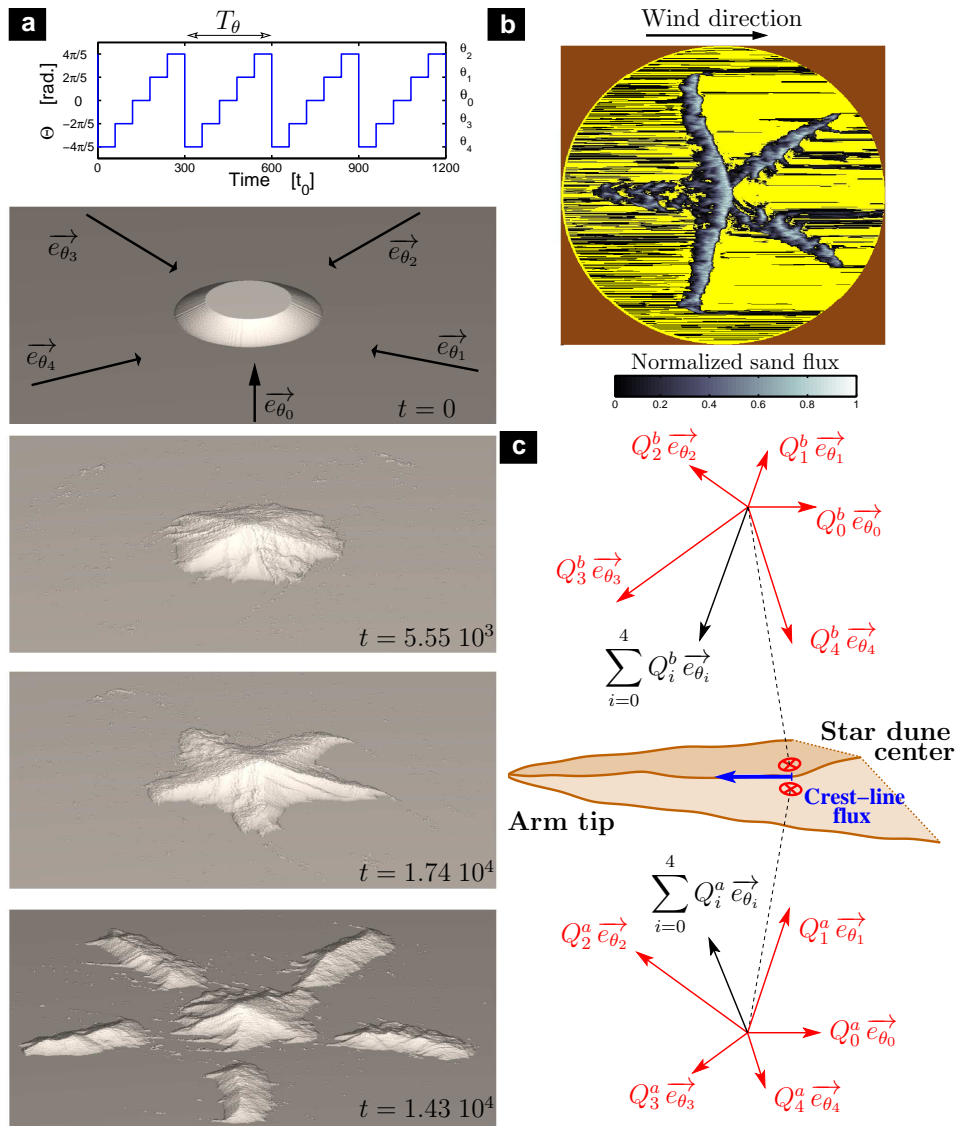
Figure 4: Arm development and sediment flux across a crestline of a star dune. (a) Formation of a 5-armed star dune by growth of longitudinal dunes using a periodic function of wind directionality with 5 wind directions (see also Fig.3 of the main manuscript). The period $T_\theta = 5t_\theta = 300\ t_0$ and the rotation angle $\theta = 2\pi/5$ are constant. (b) Sediment fluxes on the star dune at $t/t_0 = 3.6\ 10^4$. (c) For a given arm, we measure the sand flux at the crest for each wind direction. The cumulative flux yields to arm growth.

9
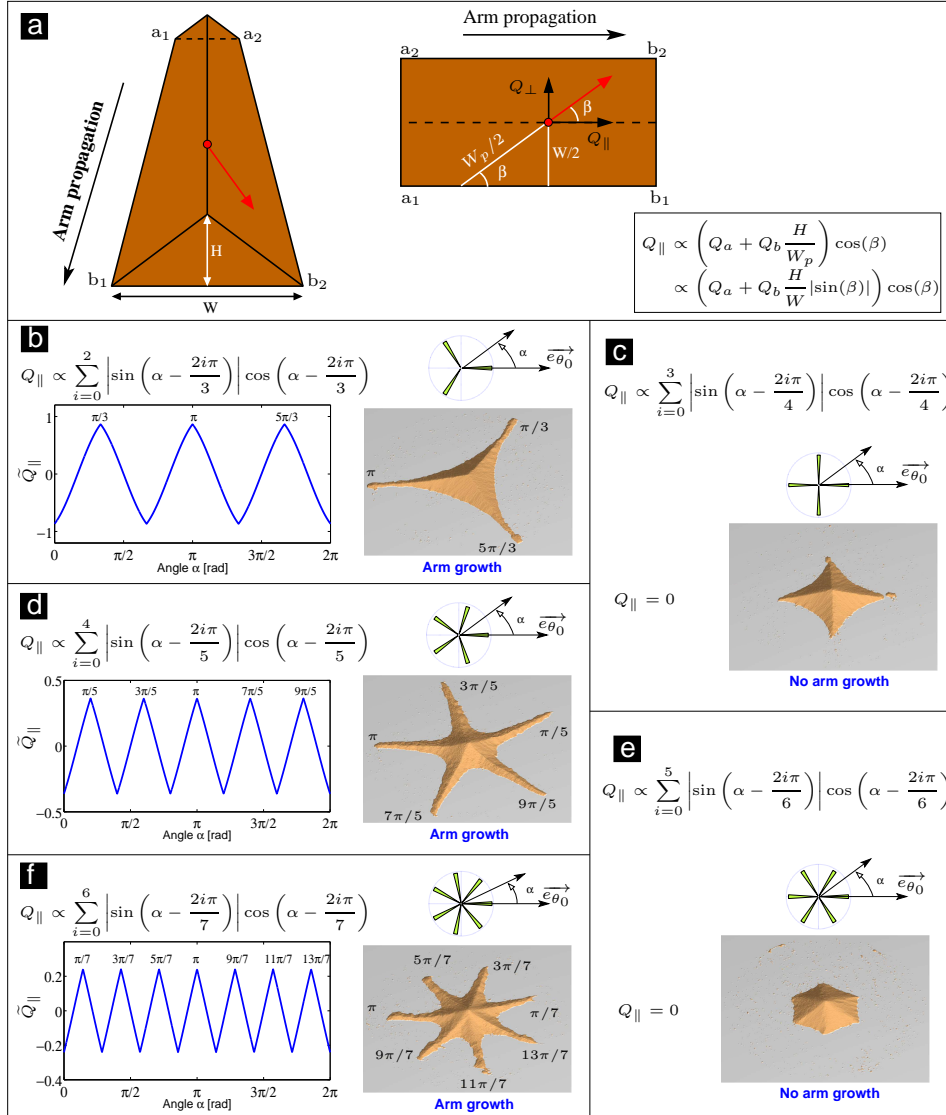
Figure 5: Comparison of analytical and numerical predictions for the direction of arm growth using periodic time functions of wind directionality with $n = \{3, 4, \ldots, 7\}$ regularly spaced wind directions, as shown by the wind roses. (a) Estimation of the sediment flux $Q_{\parallel}$ along the direction of arm growth: β is the angle between the direction of arm growth (black arrows) and the direction of the wind (red arrows); Q_a and Q_b are two constant sedimentary fluxes to take into account transport on a flat sand bed and the effect of the arm aspect ratio, respectively; H and W are the arm height and width, respectively; W_p is the apparent width of the arm along the wind direction; H/W_p is the apparent arm aspect ratio seen by the wind. From (b) to (f), we observe the perfect agreement between the analytical solutions and the outputs of the numerical model for an increasing number of wind directions. Both of them predict no arm growth for an even number of winds (c and e) and arms pointing against individual wind direction for an odd number of winds (b, d, f). Arms propagate in the direction $\alpha_i = \pi/n + 2i\pi/n$, $i = \{0, 1, \ldots, n-1\}$, for which the $Q_{\parallel}$-values are maximum.

10

3 Morphodynamics of star dune

3.1 Formation of star dune by coarsening

Fig. 3 shows the formation of a star dune by pattern coarsening (i. e. amalgamation) using a random time function of the wind directionality with five modes, $\theta_i = 2\pi i/5$ with $i \in \{0, 1, 2, 3, 4\}$. As in the main manuscript, the wind velocity and the mean time spent in each of the five directions are the same so that the mean flux of sediment is null. The bedform dynamics explore the full hierarchy of length scales, from the elementary wavelength that perturbs the initial flat sand bed to the size of the giant star dune that scales with the depth of the flow. Finally, as for the periodic wind regime, a stationary state with arms pointing against individual direction is reached when the star dunes cannot longer increase in height [*Andreotti et al.*, 2009]. Note that, whatever the number of wind directions, the stationary dune features described in the main manuscript are robust and resilient to the random time function of wind directionality.

3.2 Crest orientation and sediment flux along a radiating arm

As is systematically the case for sand dunes, the star-dune shape may be studied through the estimation of the sand flux in crestal areas [*Rubin and Hunter*, 1987]. Using the outputs of the model, we directly quantify the orientation and the magnitude of the sediment flux across the crestline by counting the number of transitions in the model of sediment transport (Fig. 4b). Fig. 4c shows that there are mirror transport properties from both sides of the crest. The resultant flux obtained by summation reveals that there is a net sediment flux oriented toward the arm tip as it is the case for isolated longitudinal dunes [*Reffet et al.*, 2010].

Fig. 5 shows the flux predicted by Eq. 1 of the main manuscript for all possible angles of arm growth. It appears clearly from the comparison between the solutions of Eq. 1 and the outputs of the numerical simulations that, in zones of low sediment availability, alignment of arms maximises the sediment flux in the direction of arm growth (Figs. 5b, 5d and 5f). In addition, both of the analytical and numerical solutions predict no arm growth when there is an even number of winds.

3.3 Effect of the frequency of wind reorientation on the morphodynamics of a star dune arm

As in the main manuscript, in all numerical simulations presented below, the initial condition is a truncated conical sand pile located in the middle of the rotating table. Its basis has a radius of $L/6 = 100\ l_0$. For the conservation of mass within the system, each sedimentary cell ejected from the rotating

11

table in the direction of the flow is reinjected randomly through a semi-circle of injection cells located along the upwind border of the rotating table.

Fig. 6 shows the development of star dunes by growth of incipient arms using a periodic function of 5 wind directionality with a period T_θ. As it is systematically the case in all simulations, arm growth directions are opposite to the individual wind directions. For an increasing T_θ-value, we observe that the arm growth rate is decreasing and that the width and the height of each arm are increasing (see also Fig. 4c in the main manuscript). To understand these behaviours we can quantify all these variables using the output of the cellular automaton model of sediment transport. For example, we can use the sedimentary structures of the star dunes produced by the model (see Fig. 4a and 4b in the main manuscript). During all the simulations, whenever a mobile sedimentary cell makes a transition to an immobile state, it records the time of this transition. This time is reset to the current time when the sedimentary cell becomes mobile again. Then, any configuration of immobile sedimentary cell at any time can be used to infer the depositional history of the mobile sedimentary layer in the model. Using these informations for star dunes produced with different periods T_θ of wind directionality, we evaluate the arm growth rate Γ_a from the radial distribution of deposition time of immobile sedimentary cells (Fig. 7). For all time periods in the past, we identify the maximum distance from the star dune centre where deposition has taken place (black envelops in Fig. 7). Two different regimes are observed during the formation and the development of star dunes in the model (Fig. 8):

- For $t/t_0 < 2 \cdot 10^4$, the entire surface of the original conical sand pile is reworked, erosion dominates and the flux at the boundary of the rotating table increases rapidly (see Fig. 9 for $t/t_0 < 10^4$). Then, incipient arm form and the boundary flux relaxes toward an equilibrium value (see Fig. 9 for $10^4 < t/t_0 < 2 \cdot 10^4$). As shown in Figs. 6 and 8, this preliminary phase is not affected by the periodic function of wind directionality: the (constant) arm growth rate and the radial patterns of sedimentation are the same for all T_θ-values.

- For $t/t_0 > 2 \cdot 10^4$, incipient arms develop with a stationary growth rate that depends on the specific time function of wind directionality. Fig. 8 shows that the arm growth rate is constant and decreases with respect to an increasing T_θ-value (see Fig. 4d in the main manuscript).

We simultaneously study the morphological properties of star dune arms. Figs. 10 and 11 show both height and width of star dune arms for $t/t_0 = 2 \cdot 10^4$ and $t/t_0 = 4 \cdot 10^4$ for various T_θ-values. These morphological properties reach a stationary and uniform regime characterised by constant values, which are controlled by T_θ. Both height and width are increasing linearly

12

with respect to an increasing T_θ-value, thereby maintaining a constant aspect ratio (see Fig. 4c in the main manuscript).

Finally, we also compare the sedimentary flux at the boundary of the rotating table (i. e. the "*free*" flux) with the sedimentary flux associated with arm growth (i. e. the "*bulk*" flux). To estimate the volumetric "*bulk*" flux we take

$$Q_{\text{bulk}} = n_a \, \Gamma_a \, \overline{H_a} \, \overline{W_a}$$

where $n_a = 5$ is the number of arms and where $\overline{H_a}$ and $\overline{W_a}$ are the average height and width of the growing arm, respectively. Fig 12 shows that the free and bulk fluxes are of the same order of magnitude and strongly anti-correlated when plotted with respect to the T_θ-value. They evolve symmetrically with respect to one another indicating that, as the T_θ-value increases, the deficit of bulk flux is compensated by an increase of the free flux across the entire domain, especially at the boundary of the rotating table. This free flux generated during period of constant wind directionality is a critical control parameter of arm growth rate.

Indeed, during periods of constant wind directionality the longitudinal arm is seen as a transverse dune. This transverse dune destabilises and breaks at the tip by the emission of small barchans.

References

Anderson, R. S., and P. K. Haff, Simulation of eolian saltation, *Science*, *241*, 820, 1988.

Andreotti, B., A two-species model of aeolian sand transport, *J. Fluid Mech.*, *510*, 47–70, 2004.

Andreotti, B., A. Fourrière, F. Ould-Kaddour, B. Murray, and P. Claudin, Size of giant dunes limited by the depth of the atmospheric boundary layer, *Nature*, *457*, 1120–1123, 2009.

Bagnold, R. A., Flow of cohesionless grains in fluids, *Philos. Trans. R. Soc. London, Ser. A*, *249*, 235, 1956.

Charru, F., Selection of the ripple length on a granular bed, *Phys. Fluids*, *18*, 121–508, 2006.

Chopard, B., and M. Droz, *Cellular automata modeling of physical systems*, Cambridge University Press, 1998.

Claudin, P., and B. Andreotti, A scaling law for aeolian dunes on Mars, Venus, Earth, and for subaqueous ripples, *Earth Plan. Sci. Lett.*, *252*, 30–44, 2006.

d'Humières, D., P. Lallemand, and U. Frisch, Lattice gas models for 3d hydrodynamics, *Europhys. Lett.*, *2*(4), 291–297, 1986.

Elbelrhiti, H., P. Claudin, and B. Andreotti, Field evidence for surface-wave-induced instability of sand dunes, *Nature*, *437*, 720–723, 2005.

Frisch, U., B. Hasslacher, and Y. Pomeau, Lattice-gas automata for the navier-stokes equation, *Phys. Rev. Lett.*, *56*(14), 1505–1508, 1986.

Hersen, P., S. Douady, and B. Andreotti, Relevant length scale of barchan dunes, *Physical Review Letters*, *89*(26), 264,301, 2002.

Iversen, J., and K. Rasmussen, The effect of wind speed and bed slope on sand transport, *Sedimentology*, *46*, 723–731, 1999.

Narteau, C., D. Zhang, . Rozier, and P. Claudin, Setting the length and time scales of a cellular automaton dune model from the analysis of superimposed bed forms, *J. Geophys. Res.*, *114*, F03,006, doi: 10.1029/2008JF001127, 2009.

Rasmussen, K. R., J. D. Iversen, and P. Rautaheimo, Saltation and wind flow interaction in a variable slope wind tunnel, *Geomorphology*, *17*, 19–28, 1996.

Reffet, E., S. Courrech du Pont, P. Hersen, and S. Douady, Formation and stability of transverse and longitudinal sand dunes, *Geology*, *38*, 491–494, 2010.

Rothman, D. H., and S. Zaleski, *Lattice-Gas Cellular Automata*, Cambridge University Press, 2004.

Rubin, D., and R. Hunter, Bedform alignment in directionally varying flows, *Science*, *237*, 276–278, 1987.

Ungar, J. E., and P. K. Haff, Steady state saltation in air, *Sedimentology*, *34*, 289–299, 1987.

Zhang, D., C. Narteau, and . Rozier, Morphodynamics of barchan and transverse dunes using a cellular automaton model, *J. Geophys. Res.*, *115*, F03,041, doi:10.1029/2009JF001620, 2010.
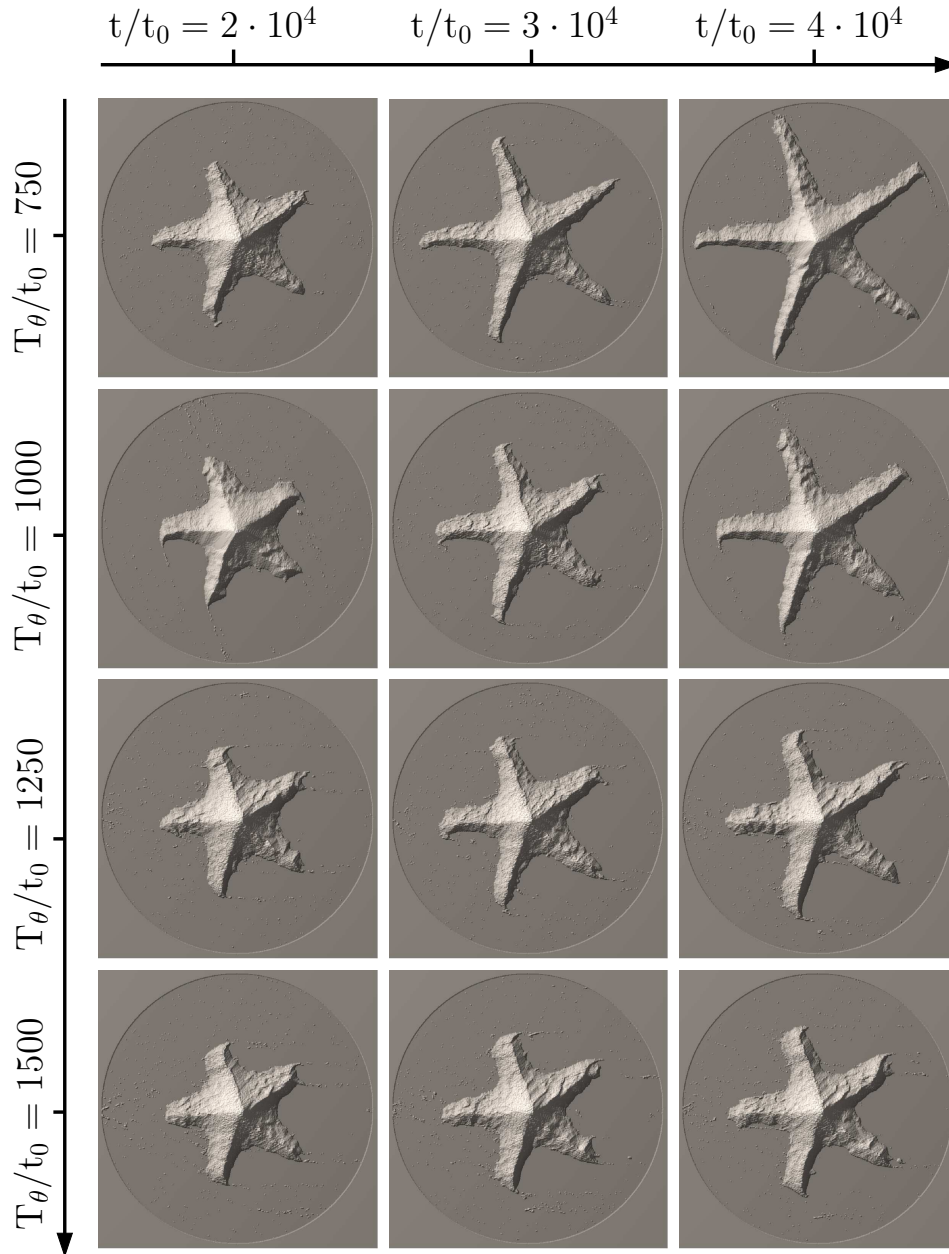
Figure 6: Growth of star dune (from the left to the right) using a periodic function of wind directionality with a period T_θ and 5 wind directions. Images have a width of 600 l_0. When the T_θ-value increases (from the top to the bottom), the arm growth rate decreases and both width and height of the arms increase, keeping the arm aspect ratio constant. Note the similitude in star-dune shape at $t/t_0 = 2 \cdot 10^4$ for all the T_θ-values.

15
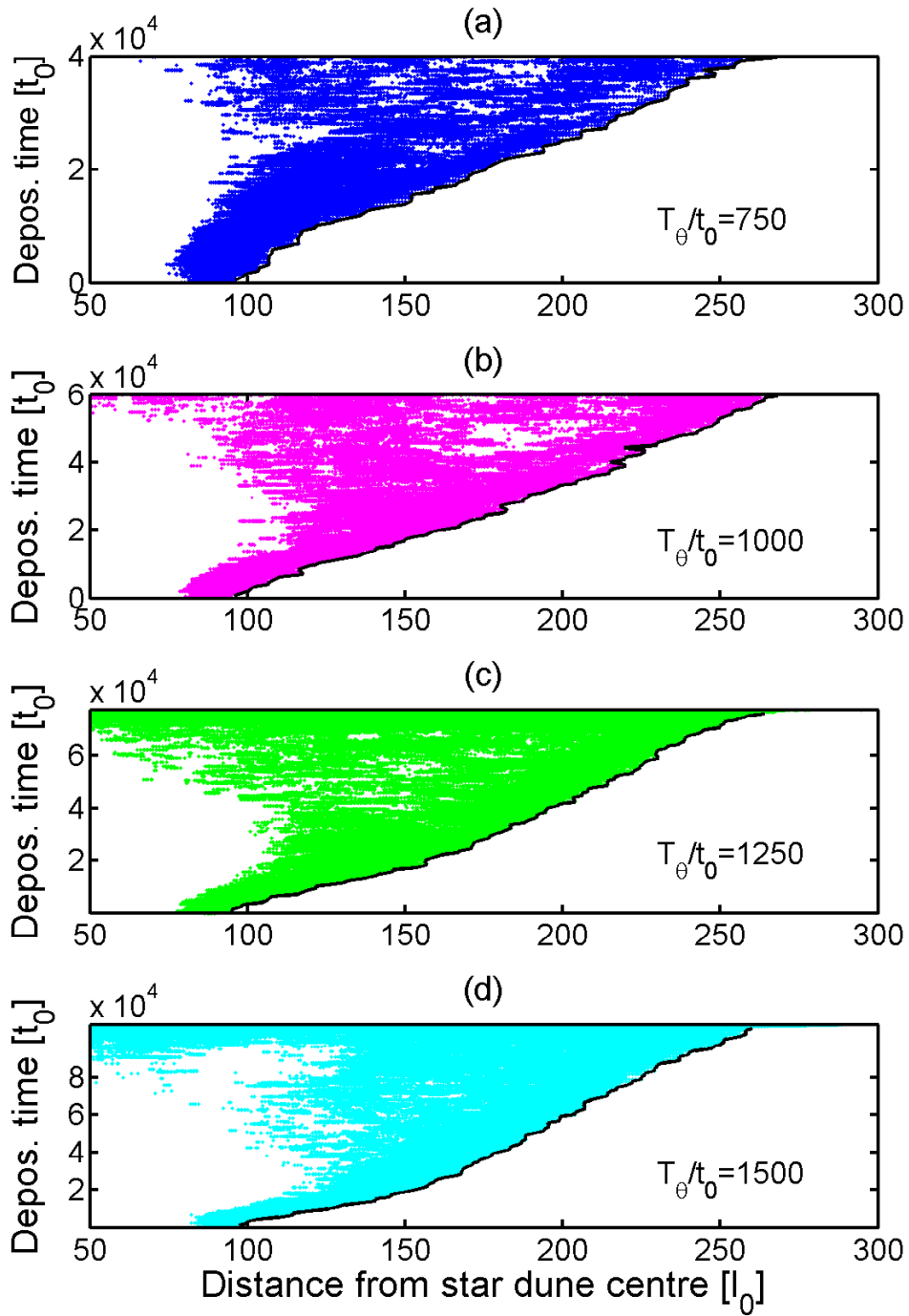
Figure 7: Deposition time of sedimentary cells with respect to the distance to star dune centre for a 5 wind regime with (a) $T_\theta/t_0 = 750$ and $t/t_0 = 4 \cdot 10^4$, (b) $T_\theta/t_0 = 1000$ and $t/t_0 = 6 \cdot 10^4$, (c) $T_\theta/t_0 = 1250$ and $t/t_0 = 8 \cdot 10^4$, (d) $T_\theta/t_0 = 1500$ and $t/t_0 = 11 \cdot 10^4$. The slope of the envelop function (black line) is inversely proportional to the arm growth rate Γ_a (see also Fig. 8).

16
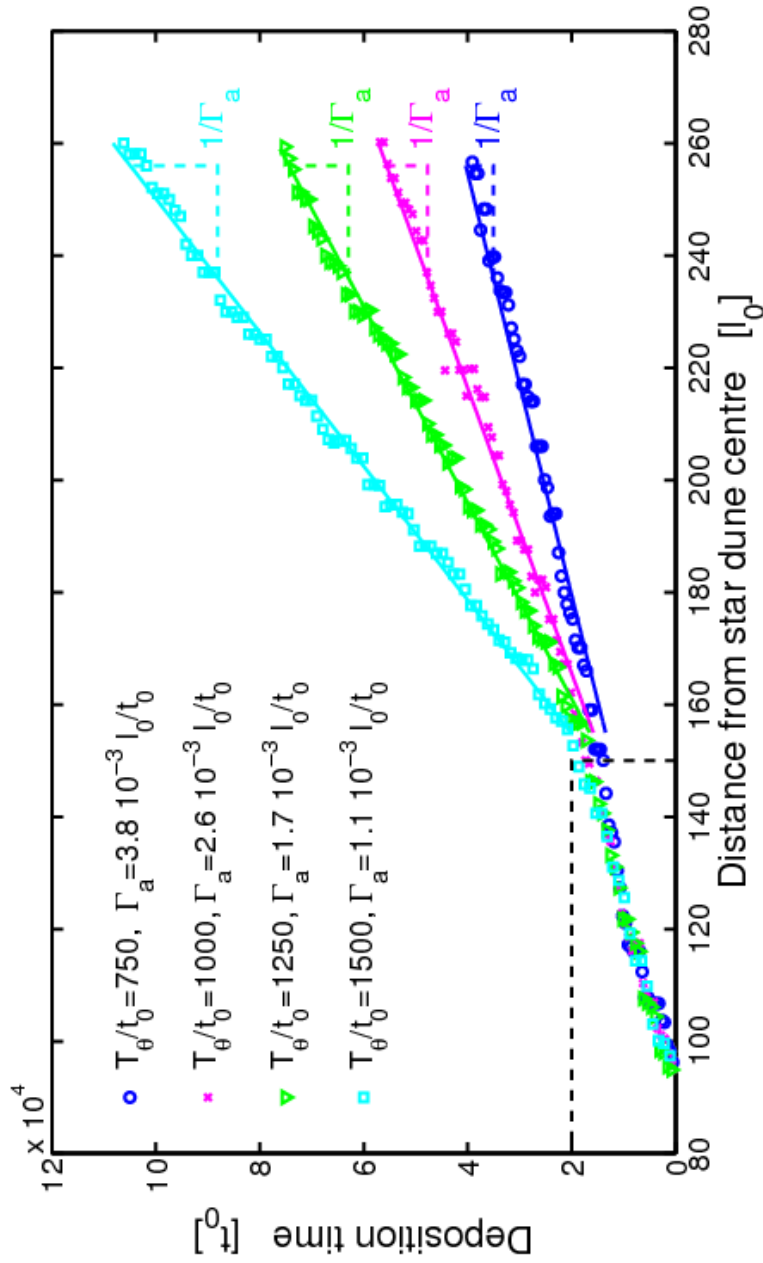
Figure 8: The envelop function of the radial deposition pattern for a 5 wind regime with different T_θ-values (black lines in Fig. 7). Two depositional regimes appear before and after $t/t_0 = 2 \cdot 10^4$ (black dashed line). For $t/t_0 < 2 \cdot 10^4$, the entire surface of the original sand pile is reworked, erosion dominates and the incipient arms form (see also Fig. 9). For $t/t_0 > 2 \cdot 10^4$, arms grow with a constant rate that depends on the periodicity of wind directionality. Because the slope is inversely proportional to the arm growth rate Γ_a (coloured dashed lines), the arm growth rate is constant and decreases with respect to an increasing T_θ-value.

17
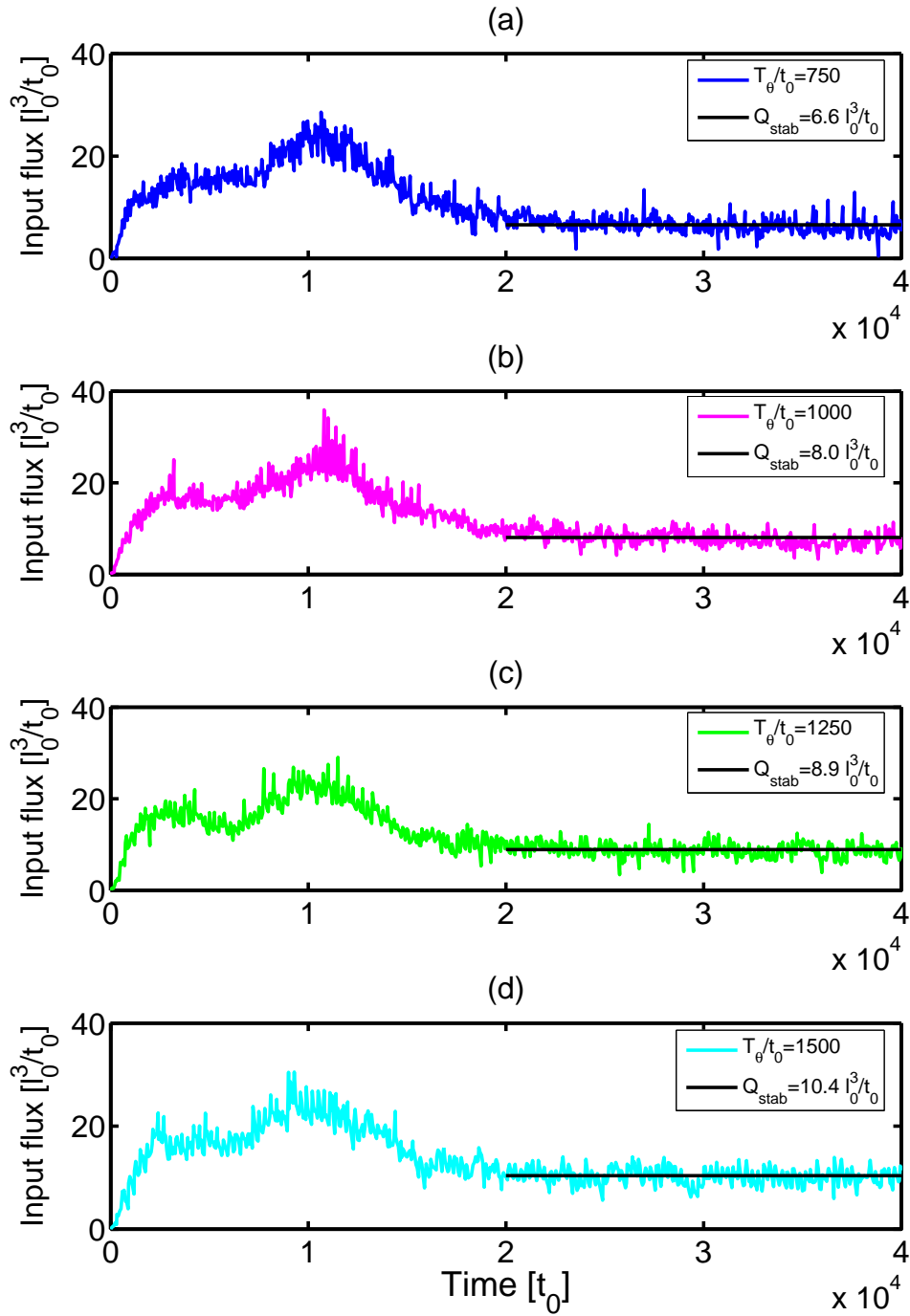
Figure 9: Flux of sedimentary cells across the boundary of the rotating table (the so-called "free flux") with respect to time for a 5 wind regime with (a) $T_\theta/t_0 = 750$, (b) $T_\theta/t_0 = 1000$, (c) $T_\theta/t_0 = 1250$, (d) $T_\theta/t_0 = 1500$. Two main regimes are observed before and after $t/t_0 = 2 \cdot 10^4$. For $t/t_0 < 2 \cdot 10^4$, the entire surface of the original sand pile is reworked, erosion dominates and the free flux increases before relaxing toward an equilibrium value. For $t/t_0 > 2 \cdot 10^4$, a constant growth rate is observed and the free flux oscillates around a stable value Q_{stab} that depends on the T_θ-value.

18
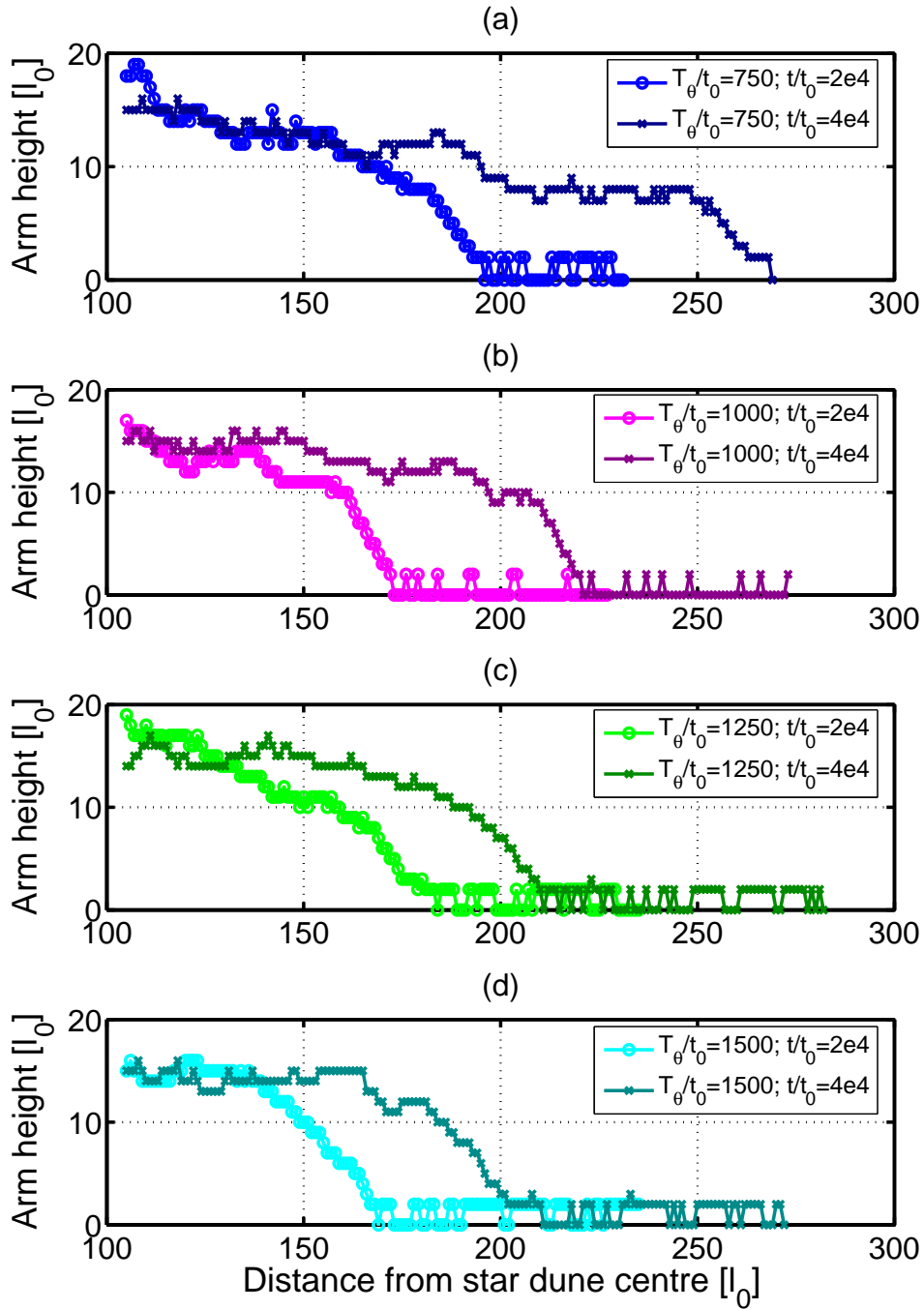
Figure 10: Height of a star-dune arm with respect to the distance from the centre of the star dune at $t/t_0 = 2 \cdot 10^4$ (light curves) and $t/t_0 = 4 \cdot 10^4$ (dark curves) for a 5 wind regime with (a) $T_\theta/t_0 = 750$, (b) $T_\theta/t_0 = 1000$, (c) $T_\theta/t_0 = 1250$, (d) $T_\theta/t_0 = 1500$. The height of the growing arm rapidly converges to a constant value that increases with an increasing T_θ-value.

19
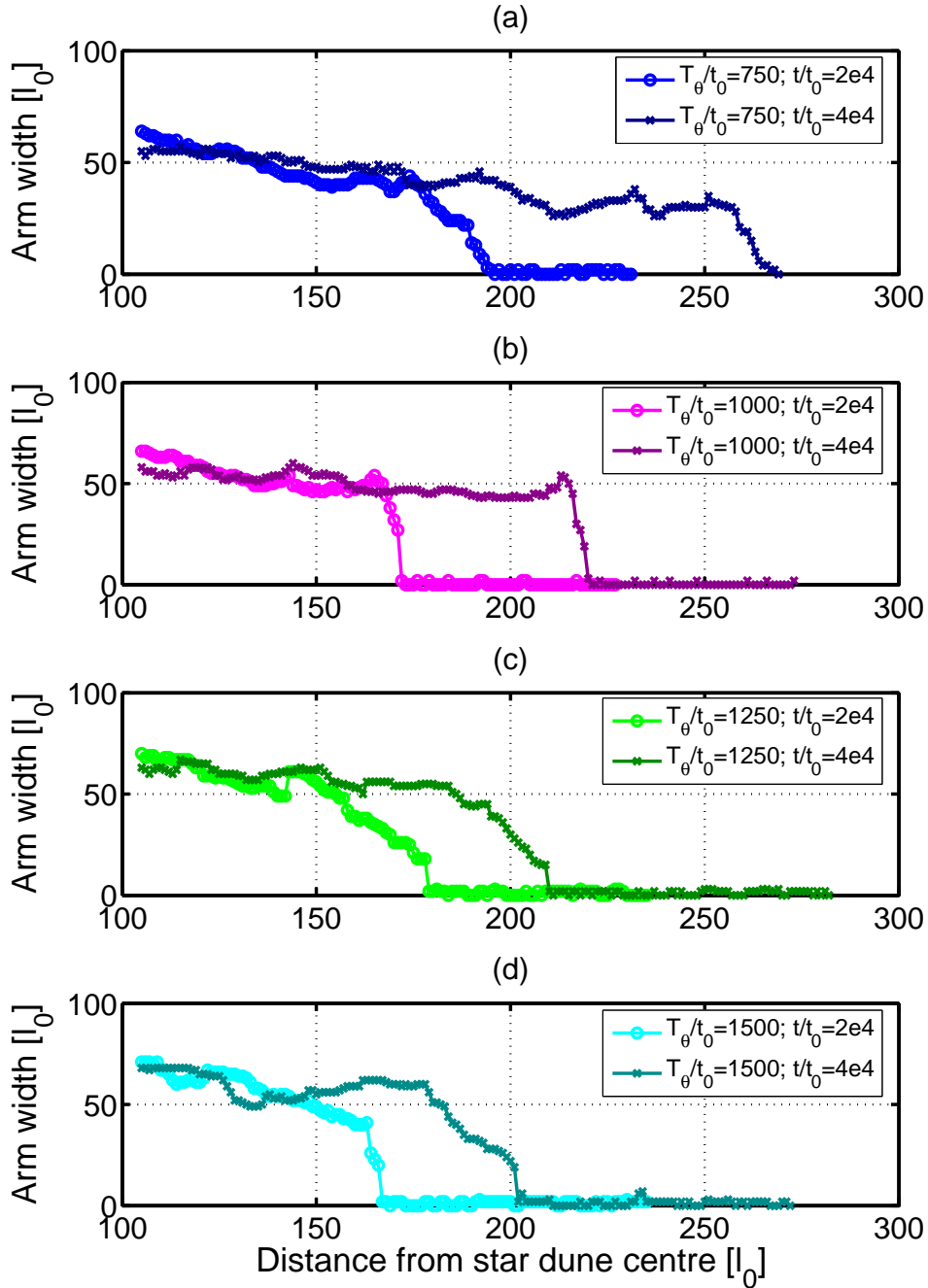
Figure 11: Width of a star-dune arm with respect to the distance from the centre of the star dune at $t/t_0 = 2 \cdot 10^4$ (light curves) and $t/t_0 = 4 \cdot 10^4$ (dark curves) for a 5 wind regime with (a) $T_\theta/t_0 = 750$, (b) $T_\theta/t_0 = 1000$, (c) $T_\theta/t_0 = 1250$, (d) $T_\theta/t_0 = 1500$. The width of the growing arm rapidly converges to a constant value that increases with an increasing T_θ-value.
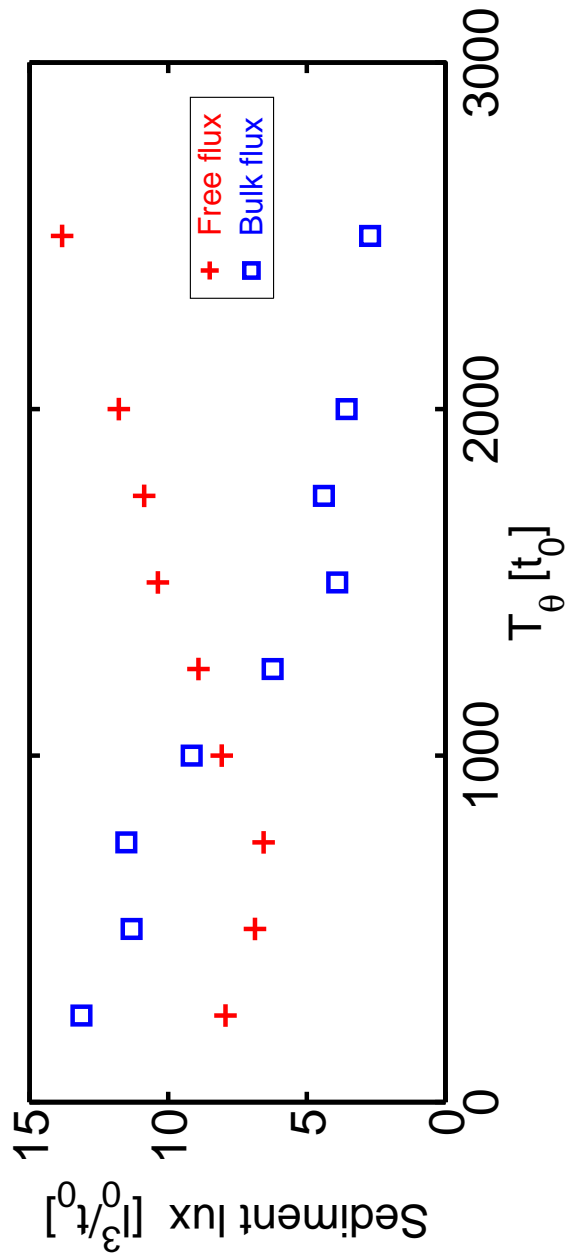
Figure 12: Flux of sediment associated with the growth of star dune arms (the so-called "bulk flux", blue squares) and across the boundary of the rotating table (the so-called "free flux", red crosses) for 5 wind regimes with respect to the T_θ-value. The strong anti-correlation and their symmetric evolution indicate that, in the model, the arm growth rate is mainly controlled by the release of sedimentary cells at the arm tip during period of constant wind orientation.

21